JOURNAL OF COMPUTATIONAL PHYSICS 77, 109–139 (1988)

A Comparative Study of Absorbing Boundary Conditions

JEFFREY G. BLASCHAK

Department of Electrical Engineering and Computer Science, Northwestern University, Evanston, Illinois 60208

AND

GREGORY A. KRIEGSMANN

Department of Engineering Sciences and Applied Mathematics, Northwestern University, Evanston, Illinois 60208

Received March 20, 1987; revised August 19, 1987

The utilization of a numerical absorbing boundary condition, which limits the domain of computation, is an important consideration in finite difference simulations of the wave equation on infinite regions. One technique for generating these conditions is based on the theory of approximate one-way wave equations. In this paper, we investigate the effectiveness of second- and third-order boundary conditions based on one-way wave equations derived from various classes of approximants. By considering two model problems, our numerical experiments indicate that one-way wave equations derived from Padé approximation perform best as numerical absorbing boundary conditions for a class of problems of interest in the simulation of electromagnetic wave propagation. © 1988 Academic Press, Inc.

1. INTRODUCTION

In this paper, we are concerned with the numerical implementation of one-way wave equations for use as absorbing boundary conditions in finite difference simulations of the wave equation. The one-way wave equations considered here are obtained from approximations of pseudodifferential operators, which result when the wave equation is factored in two-dimensional rectangular coordinates. Recent advances in the theory of one-way wave equations, reported by Trefethen and Halpern in [1, 2], have served as the motivation for this study. Also, the work of Higdon, reported in [3], has provided insights into the development of difference schemes for absorbing boundary conditions and the characterization of boundary conditions for waves which obliquely strike the boundaries.

In this paper, we present stable difference schemes for boundary conditions based on the second- and third-order one-way wave equations derived in Ref. [2]. The difference schemes are presented in a general manner, which easily incorporates the

0021-9991/88 $3.00

approximations reported in [2]. In particular, the scheme which implements third-order absorbing boundary conditions is new. The performance of the difference schemes proposed here is compared to other methods, that numerically implement one-way wave equations, reported in [3].

We investigate the effectiveness of the boundary conditions by employing them in finite difference simulations of two problems modeling electromagnetic wave propagation. The first problem involves the propagation of a pulse from a point source in a two-dimensional domain. The second problem describes the scattering of a time-harmonic plane wave from a structure of computational interest. We find that the third-order Padé boundary condition outperforms all other conditions, regardless of their order, for the pulse propagation problem. In contrast, the second-order Padé condition works best for the time-harmonic scattering problem. When the third-order Padé condition is used, a noticeably degraded solution is obtained. This degradation seems to be caused by the proximity of the scattering body to the artificial boundary.

The contents of this paper proceed as follows. Section 2 contains a summary of the wave propagation algorithm which is used to test the absorbing boundary conditions. Section 3 summarizes the application of approximation theory in the derivation of second and third-order boundary conditions. Section 4 contains the derivation of stable difference approximations, which give explicit expressions for the boundary points for both second- and third-order conditions. Section 5 includes the results of several numerical experiments which evaluated the effectiveness of the conditions for the two model problems. Finally, Section 6 contains a summary and a discussion of our experimental results.

2. The FD-TD Algorithm

The absorbing boundary conditions considered in this study are coupled to an algorithm which is particularly well suited to the study of electromagnetic wave interaction problems. The algorithm is a finite-difference time-domain (FD-TD) solution of Maxwell's equations [4–7]. For the purposes of this study, a simplified version of the this algorithm, which models two-dimensional electromagnetic wave propagation in a homogeneous free-space in the case of transverse magnetic (TM) polarization, is used. Details of the algorithm are summarized here so that the numerical implementation of the absorbing boundary conditions is easily stated and understood.

The basis of the FD-TD algorithm is Maxwell's curl equations,

$$\nabla \times \mathbf{E} = -\mu \frac{\partial \mathbf{H}}{\partial t} \tag{2.1a}$$

$$\nabla \times \mathbf{H} = \varepsilon \frac{\partial \mathbf{E}}{\partial t}, \tag{2.1b}$$

where **E** and **H** are expressed in a Cartesian coordinate system. Because we are concerned with the implementation of absorbing boundary conditions on the boundary of a homogeneous region which surrounds a scattering body, we use free-space values for μ and ε. For problems in which the fields are independent of the z coordinate and in the case having the **H** field contained completely in a plane transverse to the z axis (TM polarization), we have

$$\mathbf{E}(x, y, t) = E_z(x, y, t)\,\hat{\mathbf{z}}$$

$$\mathbf{H}(x, y, t) = H_x(x, y, t)\,\hat{\mathbf{x}} + H_y(x, y, t)\,\hat{\mathbf{y}}$$

and the curl equations reduce to

$$\frac{\partial H_x}{\partial t} = -\frac{1}{\mu}\frac{\partial E_z}{\partial y} \tag{2.2a}$$

$$\frac{\partial H_y}{\partial t} = \frac{1}{\mu}\frac{\partial E_z}{\partial x} \tag{2.2b}$$

$$\frac{\partial E_z}{\partial t} = \frac{1}{\varepsilon}\left(\frac{\partial H_y}{\partial x} - \frac{\partial H_x}{\partial y}\right). \tag{2.2c}$$

The FD-TD algorithm achieves an approximate solution of Maxwell's curl equations by discretizing the system in (2.2) into a finite difference grid comprised of rectangular unit cells of dimensions $(\Delta x, \Delta y)$ and then explicitly integrating the system forward in time at discrete time steps of length Δt. We maintain the following notation for the discretized functions on the space-time finite difference grid,

$$F(i\,\Delta x, j\,\Delta y, n\,\Delta t) = F^n(i, j),$$

where the function is evaluated at grid position, (i, j), at the nth time step.

An efficient and accurate numerical procedure is obtained by subdividing the computational domain into unit cells of the type shown in Fig. 1. The **E** and **H** field components are spatially interleaved at half-space increments and are evaluated at

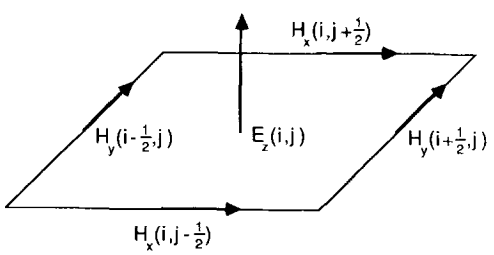

FIG. 1. FD-TD unit cell, TM polarization, two-dimensional domain.

alternate half-time steps. This arrangement permits the use of centered difference approximations for each partial derivative in the system in (2.2) resulting in compact, explicit finite difference expressions for each field component in the FD-TD grid, which are second-order accurate in both space and time increments. For this study, the system in (2.2) is discretized using uniform space increments in the x and y coordinates with the result that $\Delta x = \Delta y = \Delta$. In addition, the relation,

$$\Delta = 2c\,\Delta t \tag{2.3}$$

is chosen where c is the speed of light in free-space. The condition in (2.3) was used for algebraic convenience and to ensure that the FD-TD algorithm satisfies the Courant stability limit [8]. The result of these specifications is the following system of finite difference equations which is the discrete approximation for the system in (2.2),

$$H_x^{n+1/2}(i, j+\tfrac{1}{2}) = H_x^{n-1/2}(i, j+\tfrac{1}{2}) + \alpha[E_z^n(i, j) - E_z^n(i, j+1)] \tag{2.4a}$$

$$H_y^{n+1/2}(i+\tfrac{1}{2}, j) = H_y^{n-1/2}(i+\tfrac{1}{2}, j) + \alpha[E_z^n(i+1, j) - E_z^n(i, j)] \tag{2.4b}$$

$$\begin{aligned} E_z^{n+1}(i, j) = E_z^n(i, j) + \beta[&H_y^{n+1/2}(i+\tfrac{1}{2}, j) - H_y^{n+1/2}(i-\tfrac{1}{2}, j) \\ &+ H_x^{n+1/2}(i, j-\tfrac{1}{2}) - H_x^{n+1/2}(i, j+\tfrac{1}{2})], \end{aligned} \tag{2.4c}$$

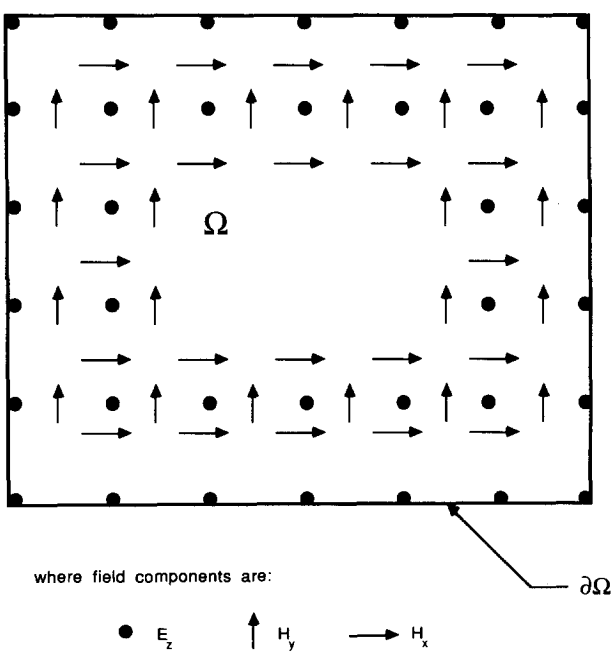

FIG. 2. Two-dimensional FD-TD computational domain and boundary, TM polarization.

where

$$\alpha = \frac{\Delta t}{\mu \Delta}, \qquad \beta = \frac{\Delta t}{\varepsilon \Delta}.$$

The computational domain used in this study was constructed as shown in Fig. 2. The **E** and **H** field points on the interior of Ω are determined using the finite difference system in (2.4). The electric field points on the boundary of the domain, $\partial\Omega$, are determined by a one-way wave equation, which is designed to prevent reflections. This approach was originally proposed by Engquist and Majda for the scalar wave equation [9] and extended by Mur for Maxwell's equations [10]. The one-way wave equations considered in this study are each used as an absorbing boundary condition for the boundary of the domain, $\partial\Omega$. Each boundary condition is implemented numerically as part of an algorithm which accurately models electromagnetic wave propagation.

3. Generalized One-Way Wave Equations

The absorbing boundary conditions evaluated in this study are based on general second- and third-order one-way wave equations. The equations are generalized in the sense that their derivation follows from the application of general rational function approximations to $\sqrt{1-s^2}$ on the interval $[-1, 1]$. In [1], Trefethen and Halpern reduced the design of one-way wave equations to such approximations and present seven families of approximants to achieve equations with improved wide-angle performance. In [1], the dispersion relations for approximate one-way wave equations were derived from which the equation, itself, follows directly. In this section, we shall derive equivalent one-way equations using operator factoring arguments.

We begin by considering the two-dimensional wave equation in Cartesian coordinates,

$$LU \equiv D_x^2 U + D_y^2 U - \frac{1}{c^2} D_t^2 U = 0, \tag{3.1}$$

where D_x^2, D_y^2, and D_t^2 denote second partial derivatives with respect to x, y, and t, respectively. Next, we factor the wave operator, L,

$$LU = L^+ L^- U = 0,$$

where L is defined as,

$$L^- \equiv D_x - \frac{D_t}{c}\sqrt{1-s^2} \tag{3.2a}$$

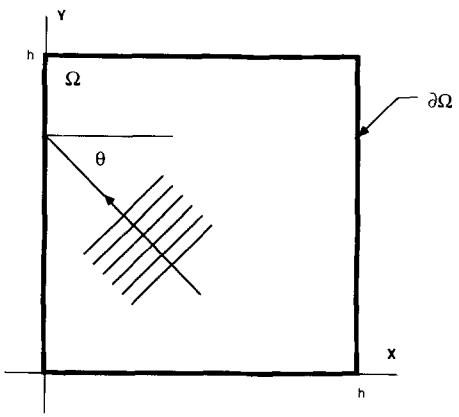

FIG. 3. Two-dimensional Cartesian computational domain.

and

$$s=\frac{cD_y}{D_t}. \tag{3.2b}$$

The operator, L^+, is similarly defined except for a "+" sign before the radical.

Engquist and Majda [9] showed that at a planar boundary at $x=0$ an application of L^- to the wave function, U, will exactly absorb plane waves incident at any angle which travel in the $-x$ direction. Thus, applying

$$L^- U=0 \tag{3.3}$$

at $x=0$ functions as an exact absorbing boundary condition which absorbs wave motion from the interior of the spatial domain, Ω, shown in Fig. 3. The operator, L^+, performs the same function for waves traveling in the $+x$ direction that impinge upon the other boundary at $x=h$. The presence of the radical in (3.2a) classifies L^- as a pseudo-differential operator because it is non-local in both the space and time variables. This is an undesirable characteristic because it prohibits the direct numerical implementation of (3.3) as an absorbing boundary condition for dimensions greater than one.

Algebraic approximations of the radical in (3.2a) produce absorbing boundary conditions that can be implemented numerically with finite difference schemes. The resulting boundary conditions are not exact in that a small amount of reflection does develop as waves pass through the boundary. Recent results suggest that it is possible to design an absorbing boundary condition which minimizes the reflection as much as possible over a range of incident angles [2]. The substitution, first proposed by Engquist and Majda [9],

$$\sqrt{1-s^2}\approx 1-\tfrac{1}{2}s^2 \tag{3.4}$$

gives the following absorbing boundary condition which can be implemented at the boundary, $x = 0$,

$$U_{xt} - \frac{1}{c} U_{tt} + \frac{c}{2} U_{yy} = 0. \tag{3.5}$$

Trefethen and Halpern [1, 2] proposed a generalization of (3.5). They showed that the construction of an absorbing boundary condition reduces to the approximation of $\sqrt{1-s^2}$ on the interval, $[-1, 1]$, by the rational function,

$$r(s) = \frac{p_m(s)}{q_n(s)}, \tag{3.6}$$

where p and q are polynomials of degree m and n, respectively. The general rational function in (3.6) is of type (m, n). By specifying a general type (2, 0) approximant,

$$\sqrt{1-s^2} \approx p_0 + p_2 s^2, \tag{3.7}$$

the second-order absorbing boundary condition,

$$U_{xt} - \frac{p_0}{c} U_{tt} - c p_2 U_{yy} = 0. \tag{3.8}$$

is obtained. The choice of the coefficients, p_0 and p_2, is determined by the method of approximation. Expressions similar to (3.8) can be derived and applied at the other three boundaries of a two-dimensional finite difference grid. Experience with the use of (3.5) shows that it works well when the grid truncation boundaries are sufficiently distant so that the scattered waves impact the boundaries at near normal incidence. Higher order approximations to the radical in (3.2a) were proposed in [2] as a means to derive more accurate absorbing boundary conditions. Using the general rational approximant of type (2, 2),

$$\sqrt{1-s^2} \approx \frac{p_0 + p_2 s^2}{q_0 + q_2 s^2} \tag{3.9}$$

gives the third-order absorbing boundary condition,

$$q_0 U_{xtt} + c^2 q_2 U_{xyy} - \frac{p_0}{c} U_{ttt} - c p_2 U_{tyy} = 0. \tag{3.10}$$

The choice of the coefficients, p and q, in (3.9) produces various families of absorbing boundary conditions as suggested in [2].

In earlier works, the radical in (3.2a) was approximated with Padé techniques [2]. For example, the two-term Taylor approximation in (3.4) is a Padé (2, 0) type approximant. By choosing, $p_0 = q_0 = 1$, $p_2 = -\frac{3}{4}$, $q_2 = -\frac{1}{4}$, a Padé (2, 2) type approximation is realized in (3.9) and the resulting absorbing boundary condition

TABLE I

Coefficients for 3rd-Order Conditions

Type of approximation	p_0	p_2	q_2	Angles of exact absorption (degrees)
Padé	1.00000	−0.75000	−0.25000	0.00
L_α^∞ ($\alpha = 45°$)	0.99973	−0.80864	−0.31657	11.7, 31.9, 43.5
Chebyshev points	0.99650	−0.91296	−0.47258	15.0, 45.0, 75.0
L^2	0.99250	−0.92233	−0.51084	18.4, 51.3, 76.6
C-P	0.99030	−0.94314	−0.55556	18.4, 53.1, 81.2
Newman points	1.00000	−1.00000	−0.66976	0.0, 60.5, 90.0
L^∞	0.95651	−0.94354	−0.70385	26.9, 66.6, 87.0

Note. $q_0 = 1.00000$ for each approximant.

is the third-order condition of Engquist and Majda [9]. Because the Padé family interpolates $\sqrt{1-s^2}$ exactly at $s=0$, the corresponding absorbing boundary conditions exactly absorb plane waves normally incident on the boundary. (See Fig. 3.)

Spreading out the angles at which the boundary exactly absorbs plane waves is postulated in [2] as a means to obtain absorbing boundary conditions having improved wide-angle performance compared to those of the Padé family. Six other techniques of approximation are presented in detail in [2] for approximants of types: (0, 0), (2, 0), (2, 2), (4, 2), and (4, 4). In addition to Padé, the techniques are: Least-squares (or L^2 which minimizes the L^2 norm of the error of the approximation on $[-1, 1]$), interpolation at Chebyshev points, interpolation at Newman points, Chebyshev (or L^∞ which minimizes the L^∞ norm), Chebyshev-Padé (or C-P), and Chebyshev on a subinterval (or L_α^∞ which minimizes the L^∞ norm on the subinterval, $|s| \leqslant \alpha$).

In the present study, we have concentrated on the numerical implementation and evaluation of type (2, 0) and (2, 2) absorbing boundary conditions. The coefficients and angles of exact absorption for seven families of type (2, 0) and (2, 2) absorbing boundary conditions are presented in Tables I and II. The derivation of these approximations can be found in [2]. In Section 5, we have evaluated the performance of the absorbing boundary conditions specified in Tables I and II.

In the present study, each approximant for the radical in (3.2a) yields a boundary condition which is exact for plane waves incident at a discrete set of angles on $[0, \pi/2]$. The resulting angles of exact absorption are a by-product of the order and type of approximant used. A more general approach, which permits the design of boundary conditions for plane waves incident at arbitrary angles, is presented by Higdon in [3, 15]. In [3], Higdon developed the boundary condition,

$$\left[\prod_{j=1}^{n}\left(\cos\alpha_j\frac{\partial}{\partial t} - c\frac{\partial}{\partial x}\right)\right]U = 0, \tag{3.11}$$

TABLE II

Coefficients for 2nd-Order Conditions

Type of approximation	p_0	p_2	Angles of exact absorption (degrees)
Padé	1.00000	−0.50000	0.00
L_α^∞ ($\alpha = 20°$)	1.00023	−0.51555	7.6, 18.7
Chebyshev points	1.03597	−0.76537	22.5, 67.5
L^2	1.03084	−0.73631	22.1, 64.4
C-P	1.06103	−0.84883	25.8, 73.9
Newman points	1.00000	−1.00000	0.0, 90.0
L^∞	1.12500	−1.00000	31.4, 81.6

where n is the order of the condition and the α_j are the angles of exact absorption. Equation (3.8) can be obtained from (3.11) in the case of $n = 2$ and a wave equation substitution, $U_{xx} = (1/c^2)\, U_{tt} - U_{yy}$, giving

$$p_0 = \frac{\cos \alpha_1 \cos \alpha_2 + 1}{\cos \alpha_1 + \cos \alpha_2} \tag{3.12}$$

and

$$p_2 = \frac{-1}{\cos \alpha_1 + \cos \alpha_2}. \tag{3.13}$$

The coefficients, p and q, in (3.10) can be generated from (3.11), in the case of $n = 3$, using the same substitution for U_{xx}. We omit these results for the sake of brevity. In fact, (3.11) serves to unify the design of absorbing boundary conditions, and each boundary condition considered here can be generated from it. Likewise, any second- or third-order boundary condition generated from (3.11) can be implemented using the difference schemes developed in the next section.

4. Difference Schemes

The numerical implementation of a one-way wave equation as an absorbing boundary condition is achieved using finite difference approximations. The difference scheme used must produce a stable simulation when coupled to the interior finite difference wave propagation algorithm. This section contains the presentation of difference approximations for the absorbing boundary conditions given in (3.8) and (3.10) which have proven to be stable in practice.

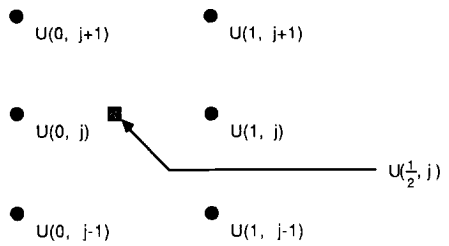

FIG. 4. Expansion point for difference schemes.

The partial derivatives in either (3.8) or (3.10) are approximated at points on the boundary of the domain. The use of centered difference formulas for derivatives which are normal to the boundary requires the knowledge of data at points exterior to the computational domain. This problem is avoided by expanding the difference formulas at a fictitious point mid-way between the boundary and the first row of interior grid points. This point is shown in Fig. 4 for a boundary at $x=0$. For the boundary point, $(0, j)$, the derivative expressions for an absorbing boundary condition are evaluated at $(\frac{1}{2}, j)$. The function at $(\frac{1}{2}, j)$ is easily related to function values at actual grid points by the simple average,

$$U\left(\frac{1}{2}, j\right)=\frac{U(0, j)+U(1, j)}{2} \tag{4.1}$$

and an explicit formula for $U^{n+1}(0, j)$ is obtained.

For the general second-order absorbing boundary condition in (3.8), the following difference approximation is readily obtained using the notions described above,

$$U^{n+1}(0, j)=\frac{1}{2p_0+1}\Lambda_1-\frac{2p_0}{2p_0+1}\Lambda_2-\frac{p_2}{4p_0+2}\Lambda_3, \tag{4.2}$$

where

$$\Lambda_1=U^{n+1}(1, j)-U^{n-1}(1, j)+U^{n-1}(0, j) \tag{4.2a}$$

$$\Lambda_2=U^{n+1}(1, j)-2U^n(1, j)-2U^n(0, j)+U^{n-1}(1, j)+U^{n-1}(0, j) \tag{4.2b}$$

$$\Lambda_3=U^n(1, j+1)-2U^n(1, j)+U^n(1, j-1)+U^n(0, j+1)-2U^n(0, j)+U^n(0, j-1). \tag{4.2c}$$

The results above are for uniform space increments, $\Delta x=\Delta y=\Delta$, and the condition, $\Delta=2c\,\Delta t$. Equation (4.2) was derived by applying centered difference

formulas at $(\frac{1}{2}, j)$ for each derivative in (3.8) and then resolving any function evaluation at midpoints with the averaging technique in (4.1).

The discretization of the third-order boundary condition, (3.10), is more subtle and involved than the second-order one. A straightforward application of centered differences yields an implicit scheme for computing the boundary data. Wishing to avoid the need for matrix inversion, we pursued the development of explicit difference scheme, which is derived as follows. We begin by multiplying (3.10) by $c\,\Delta t^2$ and then observing that the result can be written as

$$\Psi_t = c^3\,\Delta t^2\, q_2 U_{xyy}, \tag{4.3}$$

where Ψ is the auxiliary function,

$$\Psi = \frac{p_0}{c}\,\Delta t^2\, U_{tt} + cp_2\,\Delta t^2\, U_{yy} - q_0\,\Delta t^2\, U_{xt}. \tag{4.4}$$

Using centered difference formulas in (4.3) we then obtain the explicit expression

$$\Psi^{n+1}(0, j) = \frac{q_2}{4}\,\Gamma + \Psi^{n-1}(0, j) \tag{4.5a}$$

$$\Psi^0(0, j) = \Psi^1(0, j) = 0, \tag{4.5b}$$

where

$$\begin{aligned}\Gamma = {} & U^n(1, j+1) - 2U^n(1, j) + U^n(1, j-1) \\ & - U^n(0, j+1) + 2U^n(0, j) - U^n(0, j-1).\end{aligned} \tag{4.6}$$

Finally, discretizing (4.4) by centered differences, we find that $U^{n+1}(0, j)$ is given by

$$U^{n+1}(0, j) = \frac{4}{2p_0 + q_0}\left[\Psi^n(0, j) + \frac{q_0}{4}\,\Lambda_1 - \frac{p_0}{2}\,\Lambda_2 - \frac{p_2}{8}\,\Lambda_3\right], \tag{4.7}$$

where $\Lambda_1, \Lambda_2, \Lambda_3$ are defined as in (4.2).

It is interesting to observe that the scheme for the third-order condition reduces to the scheme for the second-order condition for an appropriate choice of coefficients. This can be seen by setting $q_0 = 1$ and $q_2 = 0$ in (3.9) noting that it reduces to (3.7). Then letting $q_2 = 0$ in (4.5) gives $\Psi^n(0, j) = 0$ for all n and thus (4.7) reduces to (4.2).

Other difference schemes for second- and third-order absorbing boundary conditions have been proposed by Higdon in [3]. We summarize Higdon's scheme for the second- and third-order conditions of Engquist and Majda. In [3], Higdon

proved that the nth-order Engquist and Majda condition at the $x=0$ boundary can be written as

$$\left[\frac{\partial}{\partial t}-\frac{\partial}{\partial x}\right]^n U=0, \tag{4.8}$$

with the wave speed scaled to unity. For $n=2$, (3.5) is obtained from (4.8) by using the wave equation substitution, $U_{xx}=U_{tt}-U_{yy}$. Equation (3.10), in the case of the Padé (2, 2) coefficients is obtained for $n=3$ by the same substitution. Higdon's difference approximation for (4.8) is

$$\left[\frac{I-Z^{-1}}{\Delta t}-\left(\frac{I+Z^{-1}}{2}\right)\left(\frac{K-I}{\Delta x}\right)\right]^n U^{n+1}(0,j)=0, \tag{4.9}$$

where Z and K are the shift operators,

$$Z^m U^n(i,j)=U^{n+m}(i,j)$$
$$K^m U^n(i,j)=U^n(i+m,j),$$

and I is the identity operator. Thus, for the boundary point, $(0, j)$, Higdon's scheme requires data from the boundary at earlier time steps and from the interior involving shifts only in the x direction.

Explicit expressions for $U^{n+1}(0, j)$ are now obtained from his formulas. Expanding (4.9) for $n=2, 3$ and using the condition, $\Delta x=2c\,\Delta t$, $c=1$, alternative difference schemes to (4.2) and (4.7) for the Padé (2, 0) and Padé (2, 2) conditions are obtained. For $n=2$, the result is

$$U^{n+1}(0,j)=\tfrac{16}{25}[\Lambda_1+\tfrac{1}{2}\Lambda_2-\tfrac{1}{16}\Lambda_3], \tag{4.10}$$

where

$$\Lambda_1=2U^n(0,j)-U^{n-1}(0,j) \tag{4.10a}$$
$$\Lambda_2=U^{n+1}(1,j)-U^{n-1}(1,j)+U^{n-1}(0,j) \tag{4.10b}$$
$$\begin{aligned}\Lambda_3=&U^{n+1}(2,j)+2U^n(2,j)+U^{n-1}(2,j)\\&-2U^{n+1}(1,j)-4U^n(1,j)-2U^{n-1}(1,j)\\&+2U^n(0,j)+U^{n-1}(0,j).\end{aligned} \tag{4.10c}$$

For $n=3$, the expression is

$$U^{n+1}(0,j)=\tfrac{64}{125}\Lambda_1+\tfrac{48}{125}\Lambda_2-\tfrac{12}{125}\Lambda_3+\tfrac{1}{125}\Lambda_4, \tag{4.11}$$

where

$$\Lambda_1 = 3U^n(0,j) - 3U^{n-1}(0,j) + U^{n-2}(0,j) \tag{4.11a}$$

$$\Lambda_2 = U^{n+1}(1,j) - U^n(1,j) - U^{n-1}(1,j) + U^{n-2}(1,j) + U^n(0,j) + U^{n-1}(0,j) - U^{n-2}(0,j) \tag{4.11b}$$

$$\Lambda_3 = U^{n+1}(2,j) - U^{n-1}(2,j) + U^n(2,j) - U^{n-2}(2,j) - 2U^{n+1}(1,j) + 2U^{n-1}(1,j) - 2U^n(1,j) + 2U^{n-2}(1,j) - U^{n-1}(0,j) + U^n(0,j) - U^{n-2}(0,j) \tag{4.11c}$$

$$\Lambda_4 = U^{n+1}(3,j) + 3U^{n-1}(3,j) + 3U^n(3,j) + U^{n-2}(3,j) - 3U^{n+1}(2,j) - 9U^{n-1}(2,j) - 9U^n(2,j) - 3U^{n-2}(2,j) + 3U^{n+1}(1,j) + 9U^{n-1}(1,j) + 9U^n(1,j) + 3U^{n-2}(1,j) - 3U^n(0,j) - 3U^{n-1}(0,j) - U^{n-2}(0,j). \tag{4.11d}$$

In the next section, the performance of (4.10) and (4.11) is compared to their counterparts in (4.2) and (4.7) in a model problem involving pulse propagation.

The difference schemes presented in this section are designed to implement absorbing conditions at points on the boundary other than the corners. The problem of resolving the solution at a corner has been addressed by various authors [15–17]. The corner condition, used in our numerical experiments, is now described. In the neighborhood of a corner, we assume the solution travels outward along the direction of a mesh diagonal. For a mesh cell at a corner of the domain, we compute the solution at an intermediate point which is one space increment, Δ, away from the corner point along the direction of the mesh diagonal. This is done by linear interpolation of the solution at the vertices of the corner cell. With the specification given in Eq. (2.3), the solution at this intermediate point requires two time increments to propagate along the diagonal to the position of the corner point. Thus, the corner point at the nth time step is simply the value of the intermediate point in the corner cell at the $(n-2)$th time step. This approach is similar to the approach given in [16], and has yielded a corner handling scheme that has proven to be stable in practice.

5. Numerical Experiments

This section contains the results of our numerical experiments, which were designed to evaluate the effectiveness of the absorbing boundary conditions presented in Section 3. Two groups of experiments were considered here. The first group, herein called "pulse studies," was performed to determine the reflection that a pulse produces as it propagates through a test boundary. Two measures were used for comparison. In the first, the profile of the normalized field reflected from the test

boundary was observed at a time step when the bulk of the test pulse had passed through the boundary. In the second, a measure of the total reflected error in the test domain was provided by calculating a value proportional to the L^2 norm of the reflected error at each time step. The second group of experiments, called "scattering studies," was performed to determine the steady state surface currents induced on a canonical scattering body which is illuminated by a TM polarized plane wave. The finite difference solutions in these cases are compared to a reference solution previously obtained by a numerical solution of an integral equation.

(1) *Pulse Studies*

In these studies, we measured the amount of reflection an outward propagating pulse produces as it moves through a boundary on which a one-way wave equation is applied. Figure 5a shows two domains on which the two dimensional FD-TD

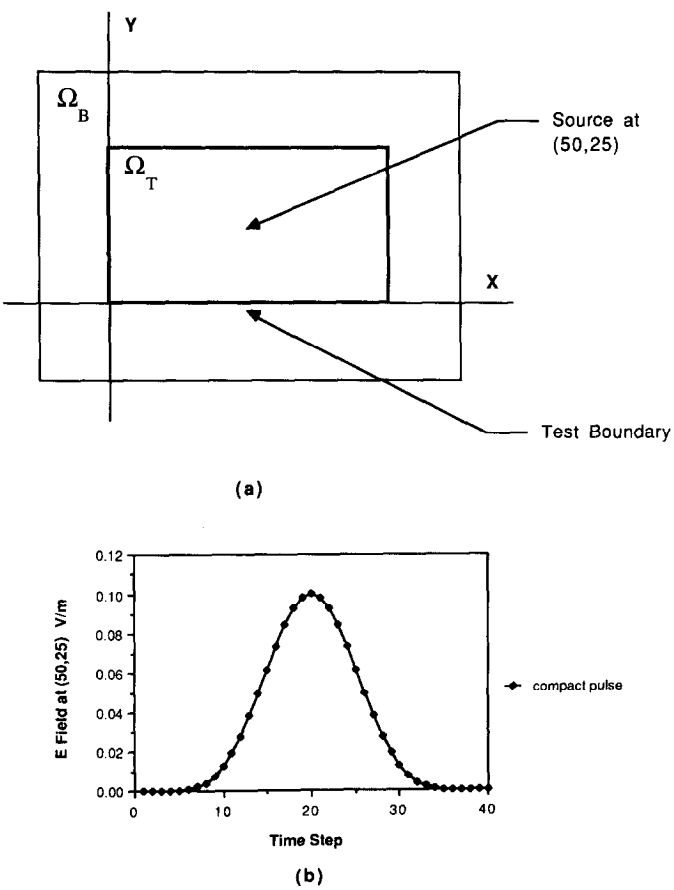

FIG. 5. Pulse studies: (a) computational domains; (b) wave source.

algorithm was computed for the transverse magnetic (TM) case. An absorbing boundary condition was applied on the boundary of the test domain, Ω_T. Each point of Ω_T was contained in the larger domain, Ω_B and a line source was located at grid position (50, 25) in Ω_B. The source produced an outward propagating cylindrical wave which was coincident in both domains until the wave first interacts with the boundary of Ω_T. Any reflection from the boundary of Ω_T made the solution, at points within the test domain, differ from the corresponding points within Ω_B. The solution at points within Ω_B represented ideal, free-space propagation until the wave reflected from its own boundary entered Ω_T. Thus, by calculating the difference between the solutions at each point and at each time step, a measure of the reflection caused by the boundary of Ω_T was obtained.

We define at the nth time step,

$$D(i, j) = E_z^T(i, j) - E_z^B(i, j) \tag{5.1}$$

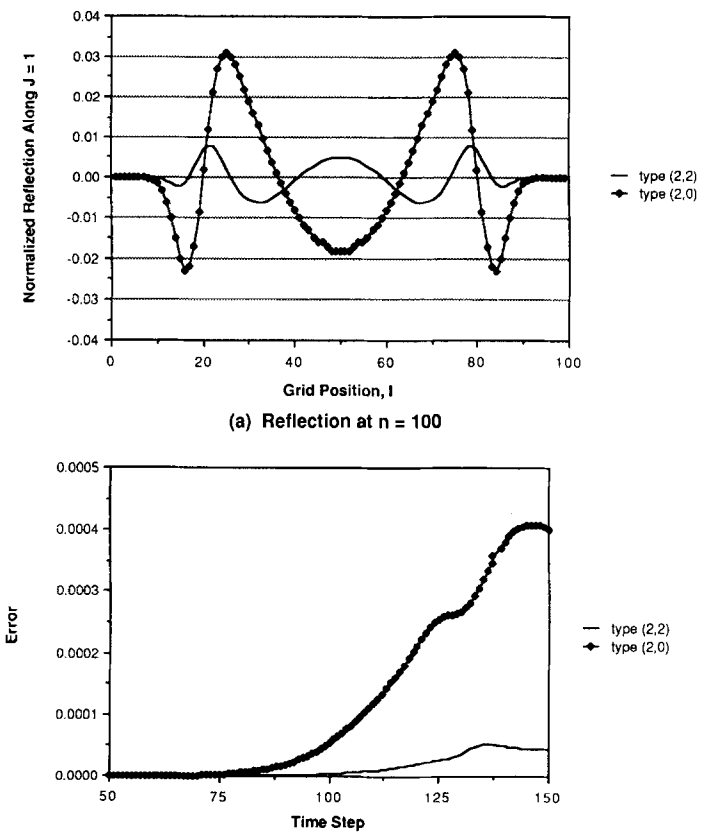

FIG. 6. Performance of Padé conditions.

for all (i, j) within the test domain, where E_z^T is the solution within Ω_T and E_z^B is the solution at points in Ω_B. Thus, $D(i, j)$ is the error at each point in the test domain caused by boundary reflections. We also define the reflected error measure,

$$E = \sum_i \sum_j D^2(i, j) \tag{5.2}$$

for all (i, j) within Ω_T which is proportional to the L^2 norm of the total reflected error within the test grid at the nth time step.

The source used in the experiments was a pulse obtained from [11]. It is defined by

$$E_z(50, 25, n) = \begin{cases} \alpha(10 - 15\cos\omega_1\xi + 6\cos\omega_2\xi - \cos\omega_3\xi), & \xi \leqslant \tau, \\ 0, & \xi > \tau, \end{cases} \tag{5.3}$$

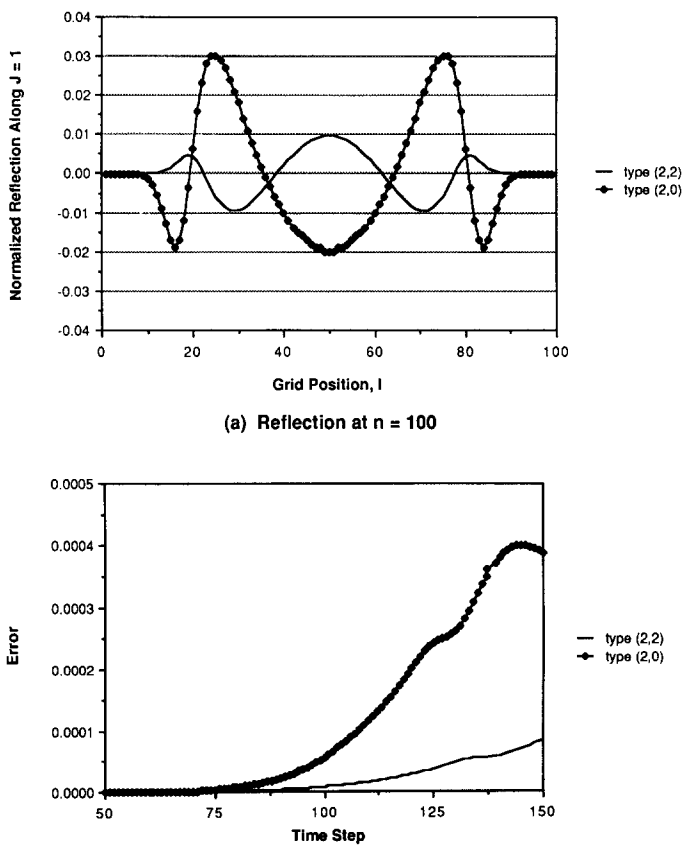

FIG. 7. Performance of L_α^∞ conditions.

where

$$\alpha = \tfrac{1}{320},$$

$$\omega_m = \frac{2\pi m}{\tau}, \qquad m = 1, 2, 3,$$

$$\xi = n\,\Delta t,$$

$$\tau = 10^{-9},$$

and Δt is the time step used in the simulation. In all experiments, Δt was taken as

$$\Delta t = 2.5 \times 10^{-11}\ \text{s}$$

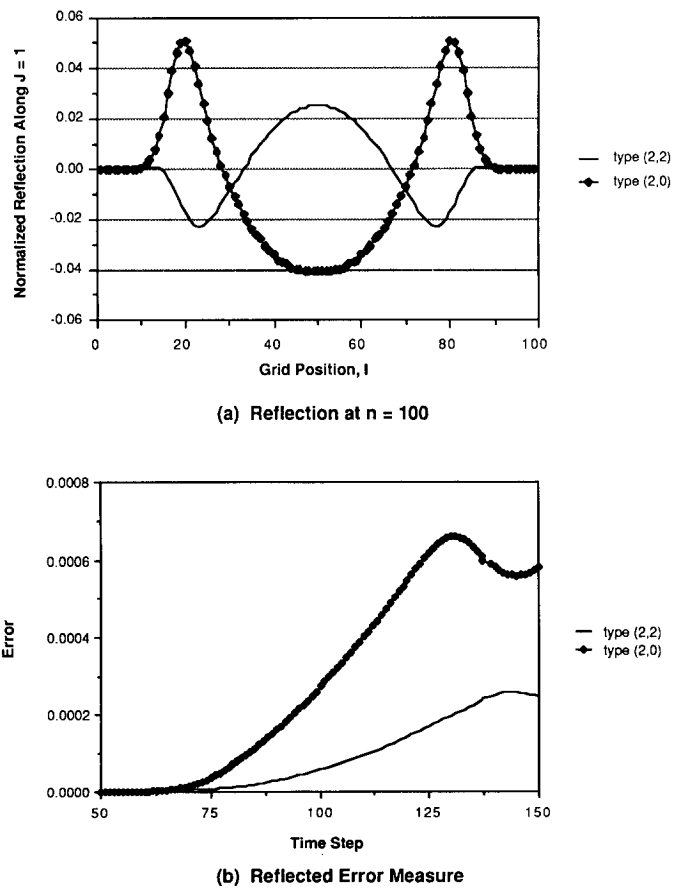

FIG. 8. Performance of L^2 conditions.

and

$$\Delta = 2c\,\Delta t, \tag{5.4}$$

where c is the speed of light in free-space and Δ is the spatial increment of the finite difference grid. The profile of the pulse defined in (5.3) is shown in Fig. 5b. This pulse was selected because it is extremely smooth. As discussed in [11], the first five derivatives of the pulse vanish at $\xi = 0$ and $\xi = \tau$. Thus, (5.3) is a good approximation to a smooth compact pulse.

The source point in Fig. 5a is 25 cells from the boundary at $y = 0$. With the specification in (5.4), disturbances at the source point required 50 time steps to propagate to the boundary at $y = 0$. Similarly, the peak of the pulse struck the boundary at the 70th time step. The reflection was observed at the first row of grid

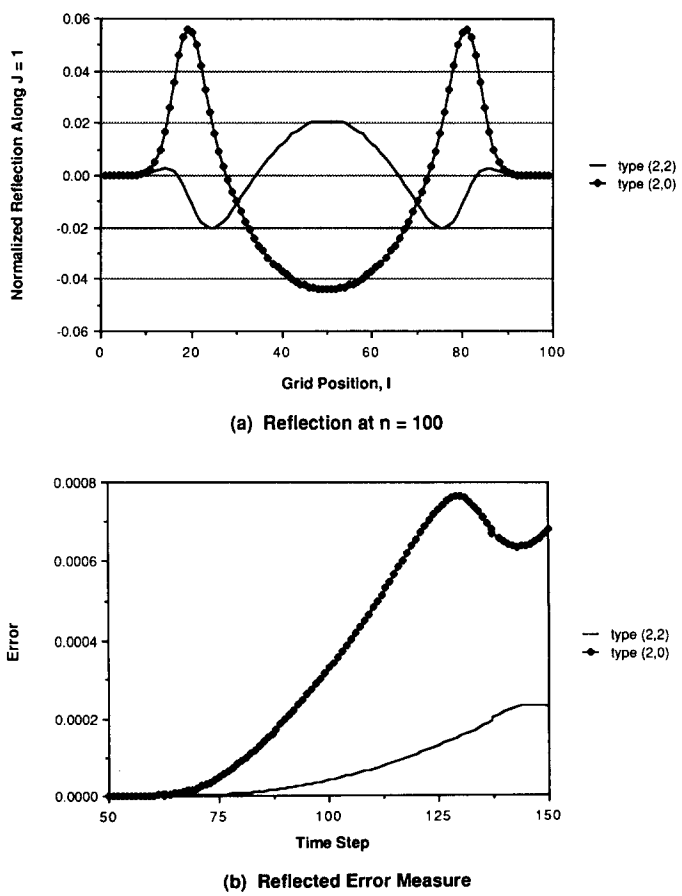

FIG. 9. Performance of Chebyshev points conditions.

points away from the $y = 0$ boundary along $J = 1$ (i.e., $D(i, 1)$) at time step, $n = 100$. This permitted the bulk of the pulse to pass through the boundary and yielded the largest observable reflection. The elongated boundary of Ω_B was taken to be 25 cells beyond the $y = 0$ boundary of Ω_B. At the time step, $n = 150$, reflections from the outer boundary just begin to enter the region of Ω_B coincident with Ω_T. Therefore, (5.2) is a valid measure of reflection solely from the boundary of Ω_T until this time step.

The results of these experiments are presented in Figs. 6 to 15. Figures 6 to 12 illustrate the results for each absorbing boundary condition defined in Tables I and II, and are arranged in order of decreasing performance. The scales of the plots are adjusted to show the wide range of observed boundary reflections and to compare, on the same scale, the performance of second- and third-order conditions for each class of approximation. The boundary conditions were implemented using the dif-

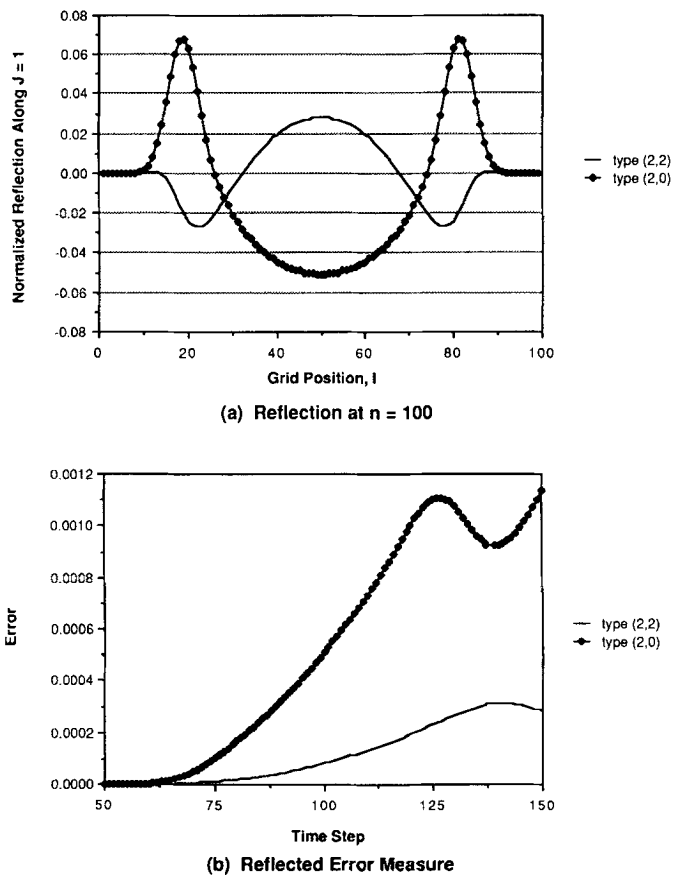

FIG. 10. Performance of Chebyshev–Padé conditions.

ference schemes presented in (4.2) and (4.7). Figures 6a to 12a show the normalized values of $D(i, 1)$ at time step, $n = 100$. The plots are normalized to the peak value of the incident pulse which strikes the $y = 0$ boundary at position (50, 0). Figures 6b to 12b show the reflected error measure defined in (5.2). Figure 13 shows a comparison between the performance of the Padé (2, 2) and the L_x^∞ (2, 2) conditions. These are observed to be the two best performing third-order conditions. The results presented in Figs. 6 to 12 indicate that the third-order conditions perform much better in the measures defined here than their second-order counterparts for each family of approximants derived in [2].

The issue of mild instabilities, caused by boundary conditions of third-order (or higher) and incident waves containing frequency components at or near the zero frequency, has been raised by Higdon in [3]. Figures 14 and 15 compare the performance of second- and third-order Padé conditions obtained using Higdon's

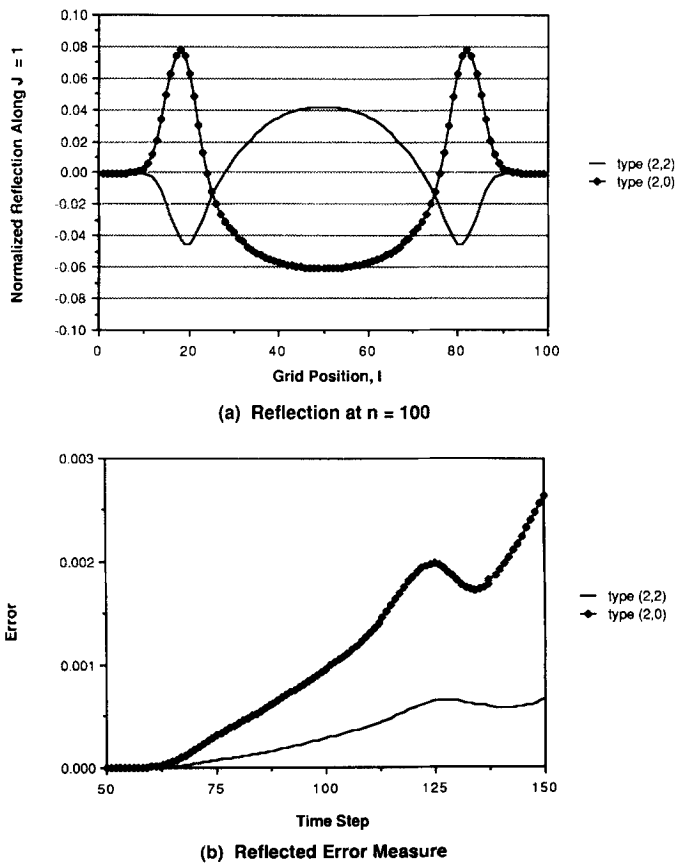

FIG. 11. Performance of L^∞ conditions.

schemes, (4.10) and (4.11), and the schemes developed in the present work, (4.2) and (4.7). For the Padé (2, 0) condition, (4.2) and (4.10) perform approximately the same. For the Padé (2, 2) condition, (4.7) performs much better than (4.11). The conclusions presented in Section 6 of [3] are evident in the model problem presented here. The scheme, (4.11), does produce much larger boundary reflections than the scheme for the second-order condition, (4.10). However, the scheme, (4.7), remained stable when excited by the same incident wave, (5.3), which has significant low frequency content. It is apparent that (4.7) avoids the instabilities noted in [3] for third-order conditions at least for this test problem. However, Higdon has recently proposed [15] a new discretization for (4.8), replacing (4.9), but has not presented numerical results for the case of a third-order boundary condition. We have implemented his new scheme, in the case of the third-order Padé boundary condition, for this test problem and have found that it does avoid the previously observed instability while yielding results comparable to ours (Fig. 6).

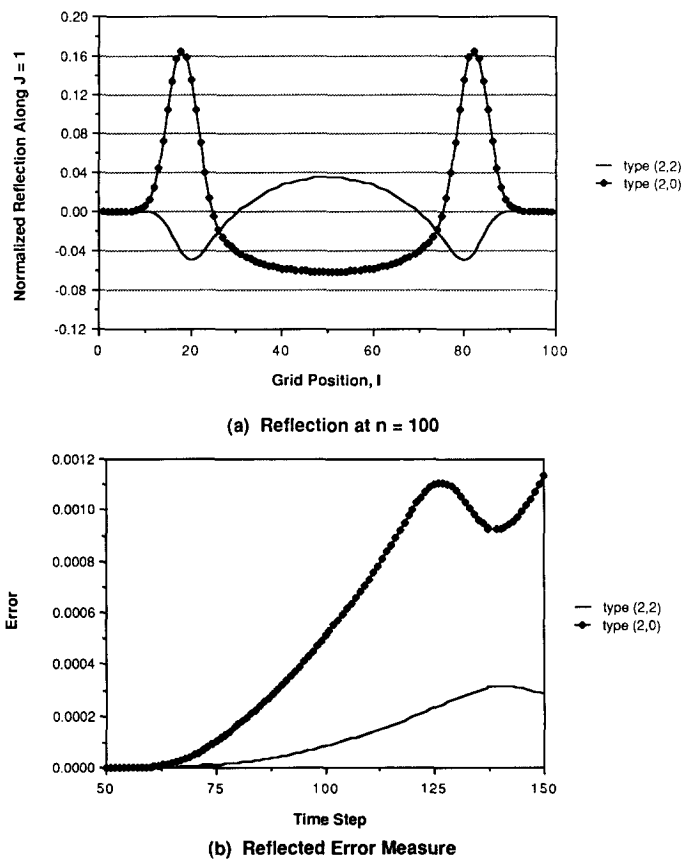

FIG. 12. Performance of Newman points conditions.

(2) *Scattering Studies*

In this group of experiments, the absorbing boundary conditions presented in Section 3 were used in the calculation of electromagnetic wave scattering from a structure of computational interest. The scattering body was taken as a perfectly conducting cylinder of square cross section and it was illuminated by a TM polarized plane wave. The incident plane wave impinged on the cylinder at an angle of ϕ^i as shown in Fig. 16. We considered two cases, $\phi^i = 0°$ (broadside incidence on side a-b) and $\phi^i = 45°$.

A quantity of physical interest in this problem is the steady state electric current density induced on the surface of the cylinder. The solution to this problem is well known. Mei and Van Bladel present numerical solutions, of an integral formulation of this problem in [12, 13], for cylinders of various electrical sizes for both TM and

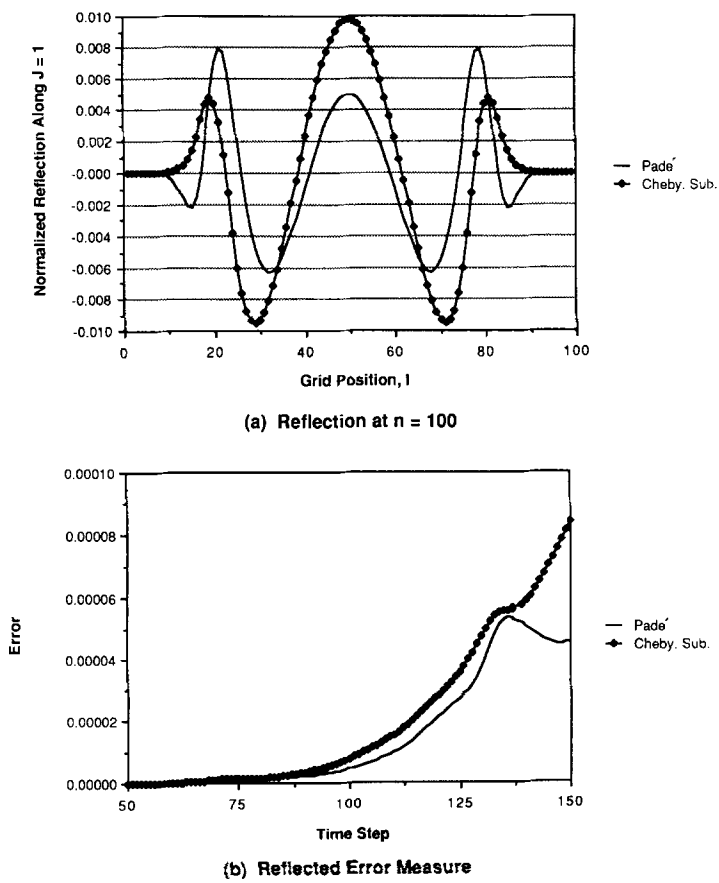

FIG. 13. Comparison of two best 3rd-order conditions.

TE polarizations. Taflove and Umashankar solved this problem in the TM case, using the FD-TD algorithm and the Padé (2, 0) boundary condition in [14], for a cylinder of electrical size, $k_0 A_s = 1$. Here, A_s is the half-width of one side and k_0 is the free space propagation constant. In this study, we reproduced their results for the surface current on sides a-b and d-c, in the case of $\phi^i = 0°$, and on sides a-b and b-c, in the case of $\phi^i = 45°$, and used them as reference solutions.

In our experiments, the cylinder was illuminated by a plane wave at 300 Mhz having a free-space wavelength of 1 m. Each side of the cylinder spanned 20 FD-TD cells. The space increment, Δ, was selected so that the half-length of each side, A_s, gave $k_0 A_s = 1$. In presenting the results, we plot the magnitude of the surface current density normalized to the magnitude of the incident magnetic field (i.e., $|K_z|/H^i$). Details pertaining to the calculation of induced surface currents using the FD-TD solution can be found in [14].

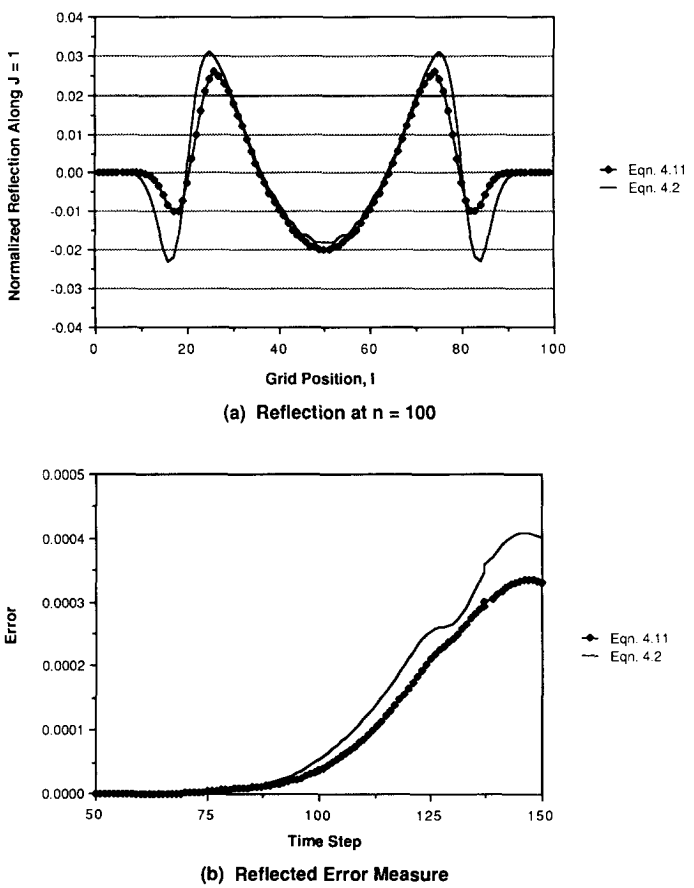

FIG. 14. Comparison of difference schemes for Padé (2, 0) condition.

In the first group of experiments, the cylinder was located within a 50×50 grid with $\phi^i = 0°$. Each side of the cylinder was positioned 15 cells from the boundary. The results are presented in Fig. 17 for the Padé conditions and in Fig. 18 for the L_α^∞ conditions. On the front face of the cylinder (broadside), the cell nearest corner "a" corresponds to position 0 on the graphs and corner "b" corresponds to position 20. On the back face (shadow region), the cell nearest corner "d" corresponds to position 0 on the graphs while corner "c" corresponds to position 20. In this group of experiments, the Padé (2, 0) result corresponds to the reference solution. Both the Padé and L_α^∞ conditions give good results in the broadside region. The third-order conditions appear to underestimate the solution in the shadow region with L_α^∞ (2, 2) performing marginally worse than Padé (2, 2). This result is unexpected and will be addressed in Section 6.

In the second group of experiments, the cylinder was positioned within a 46×46

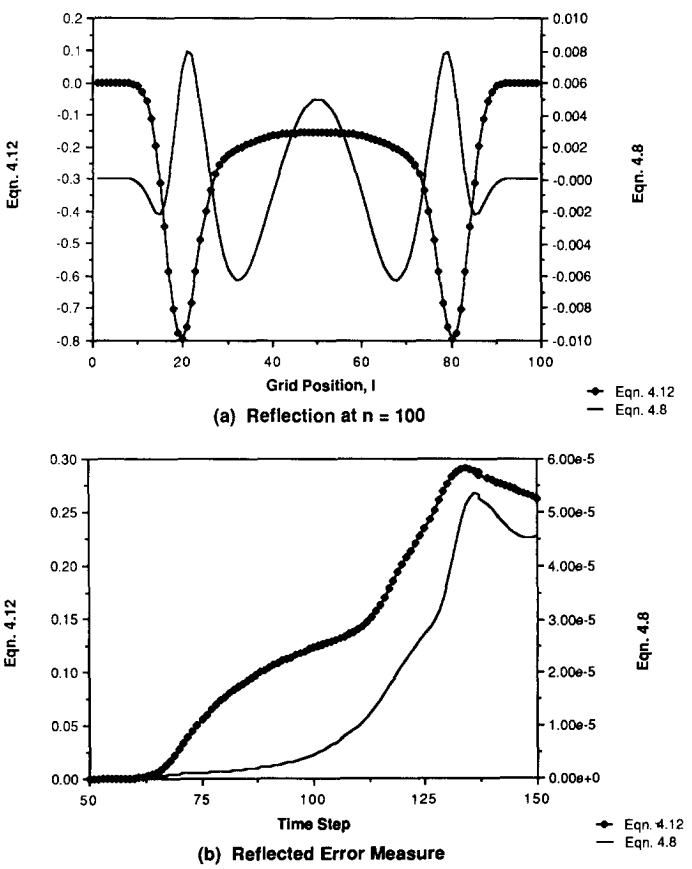

FIG. 15. Comparison of difference schemes for Padé (2, 2) condition.

contracted grid with $\phi^i = 0°$. The objective was to determine if a third-order condition could be used successfully on a smaller domain in a situation where a second-order condition produced a degraded solution. Figures 19 and 20 show results for the Padé and L_α^∞ conditions. In these experiments, sides a-b and d-a were positioned 13 cells from the boundary. In the broadside region, the (2, 0) conditions produced solutions which were degraded from the reference. The degradation is most noticeable near the corners of the cylinder. The (2, 2) conditions produced solutions which were similarly degraded and were unsatisfactory in the shadow region. Specifically, the surface current density was underestimated along the entire backside of the cylinder. The solutions obtained with the (2, 0) conditions were also unacceptable, but did not degrade as dramatically.

In the final group of experiments, the cylinder was located within a 50×50 grid with $\phi^i = 45°$. The objective was to employ the boundary conditions in a situation where the reflected waves from the cylinder struck the boundary at angles far from normal incidence. In the previous experiments with $\phi^i = 0°$, a strong reflection from side a-b interacted with the $x = 0$ boundary at normal incidence. At $\phi^i = 45°$, strong reflections from sides a-b and a-d strike the $x = 0$ and $y = 0$ boundaries at 45°. Figure 21 shows results for the Padé (2, 0) and the L_α^∞ (2, 2) conditions. One of the angles of exact absorption for the L_α^∞ (2, 2) condition is near 45°. The results show that both boundary conditions give excellent results, which include diffractive effects at the corners of the cylinder. From this experiment, it is difficult to discern any significant difference between the use of either boundary condition.

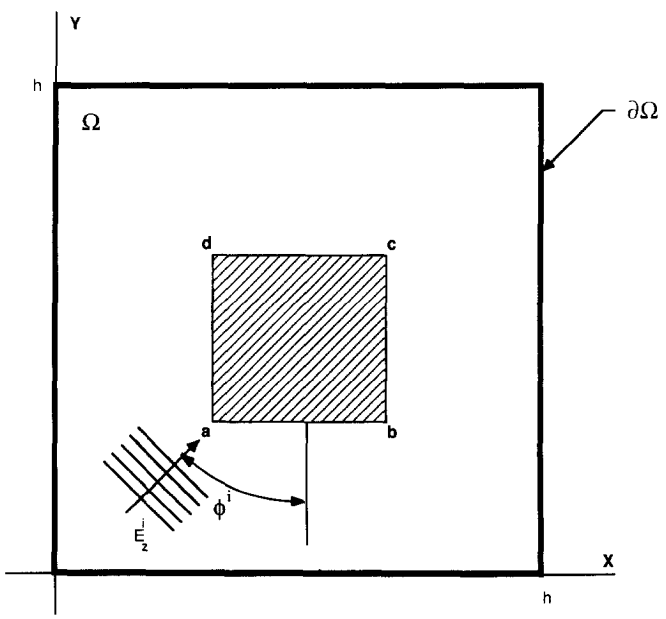

FIG. 16. Perfectly-conducting square cylinder illuminated with TM polarized plane wave.

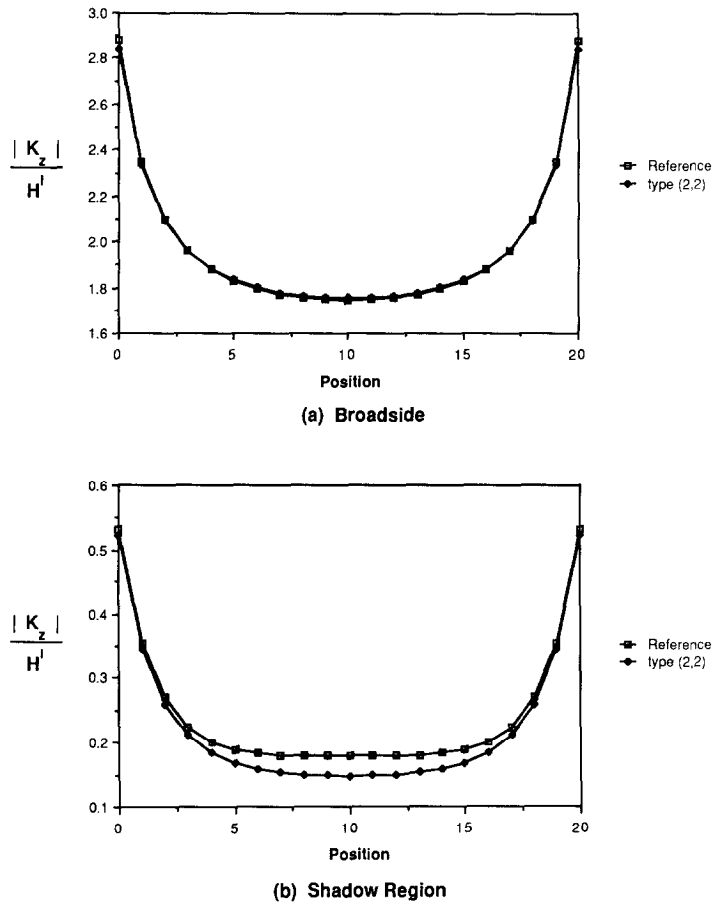

FIG. 17. Padé conditions, 50×50 grid.

6. DISCUSSION OF RESULTS

The results of the pulse studies show that third-order absorbing boundary conditions, implemented with the scheme given in (4.7), produce less reflection than their second-order counterparts. The pulse study experiments were designed to evaluate their performance in a situation where waves interact with the boundary over a wide range of incident angles while the wave source remains distant from the boundary. The Padé conditions, which are designed to accurately absorb waves at near normal incidence, performed best in this situation. This is because the incident field strength is largest at those boundary points where the incident wave is nearly normal. At the other boundary points, the field strength is smaller due the cylin-

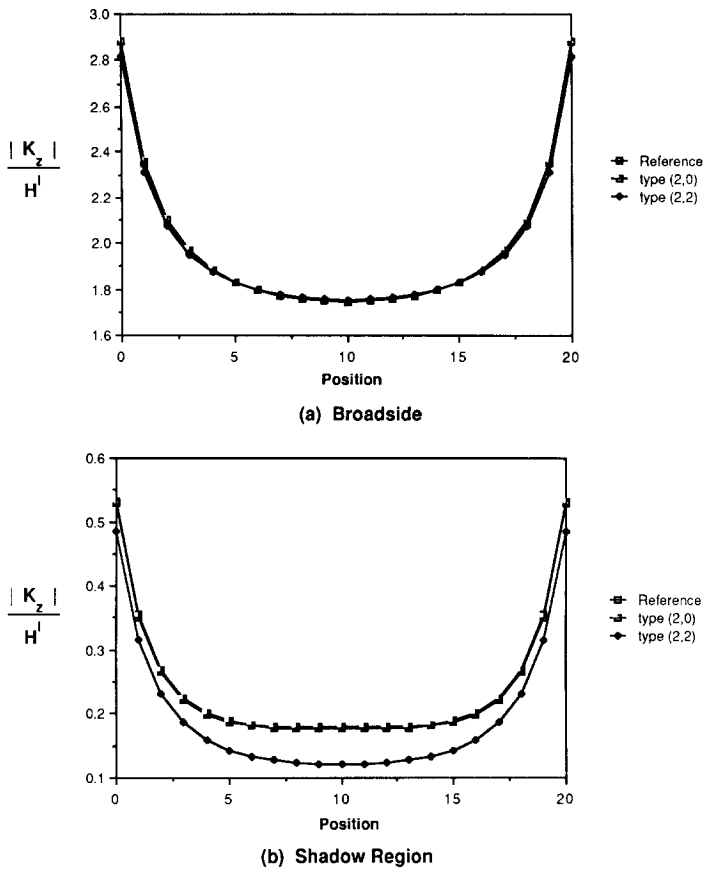

FIG. 18. L_x^{∞} conditions, 50×50 grid.

drical spreading of the incident wave. Therefore, the other boundary conditions, which sacrifice accuracy at normal incidence for performance at other angles, produce larger reflections. Our results indicate that, for problems of this type, higher order Padé boundary conditions may be helpful in further reducing spurious boundary reflections.

The scattering experiments were much more demanding than the pulse studies on the boundary conditions. This is because the waves interact several times with the boundaries before a time-harmonic state is reached. Thus, boundary reflections tend to compound numerical errors. These errors do not appear on the illuminated portion of the cylinder, where the current is primarily induced by the incident plane wave. However, the current in the shadow region is produced by the diffraction of the incident wave by the cylinder corners. It is much smaller in amplitude. The

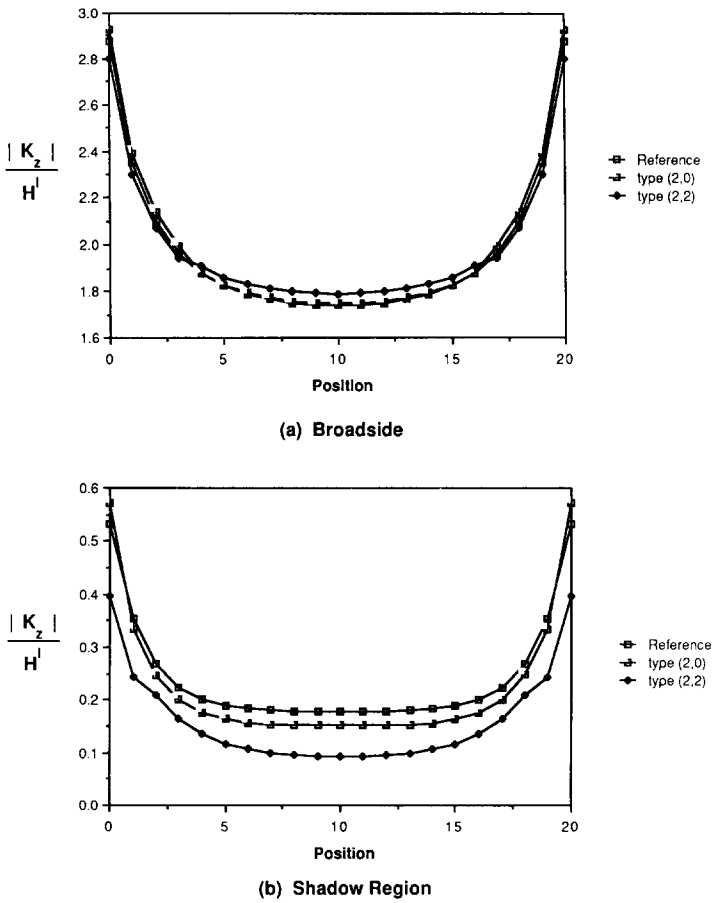

FIG. 19. Padé conditions, 46×46 grid.

solution in the shadow region is more sensitive to the effects of spurious boundary reflections which act as additional, inward propagating wave sources and induce non-physical currents on the cylinder.

produce more reflections than second-order conditions. This was clearly evident from the errors in the shadow region solution. However, in the case of $\phi^i = 45°$, the incident wave illuminates a larger portion of the cylinder, which produces larger currents in the shadow region. Thus, it was more difficult to detect the effects of boundary reflections in the shadow region for the either the Padé or the L_α^∞ conditions.

In the experiments with $\phi^i = 0°$, the boundaries were positioned less than $\frac{1}{4}$ wavelength from the scatterer, which was consistent with the simulations reported

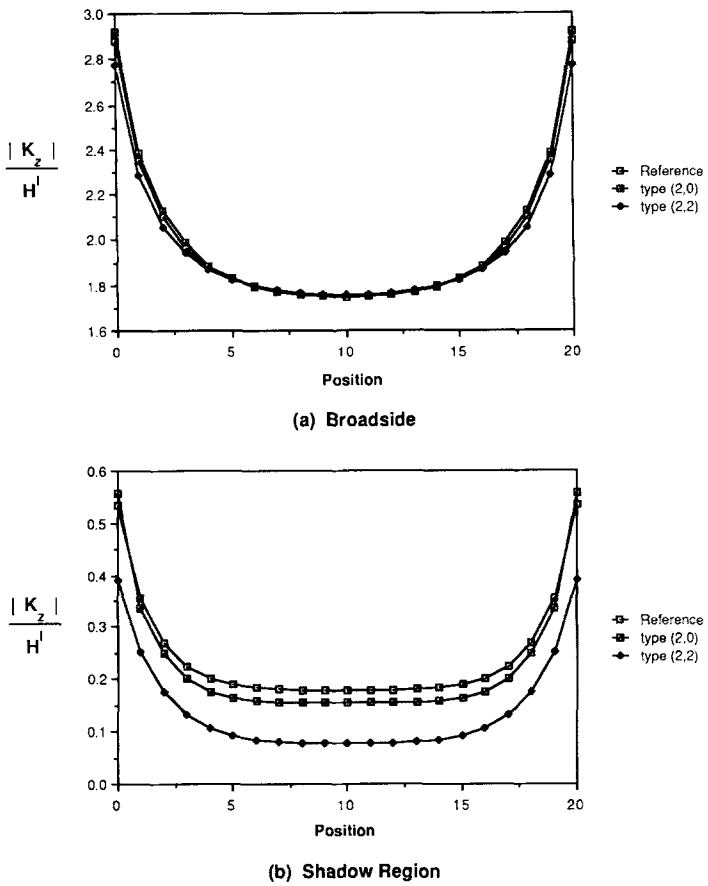

FIG. 20. L_α^∞ conditions, 46×46 grid.

in [14]. The boundary conditions were applied in the near field regime where the scattered field is strongly characterized by the outward propagating cylindrical waves generated by corner diffraction. The boundary conditions tested were designed to absorb outward propagating plane waves. When these were required to operate on cylindrical waves, the boundary operators introduced errors which were larger for the third-order conditions. We believe that these are caused by truncation errors. For third-order conditions, the truncation error generated by taking a third-order spatial derivative is $O(\Delta^2/\tau^{9/2})$. Whereas, in a typical second-order condition, the error, for taking a second-order spatial derivative, is $O(\Delta^2/\tau^{7/2})$. Thus, when these conditions are applied near a corner of the target, where $r = 0$ for the diffracted wave, the third-order condition generates larger errors. In contrast, this phenomenon was not experienced in the pulse studies because the waves experien-

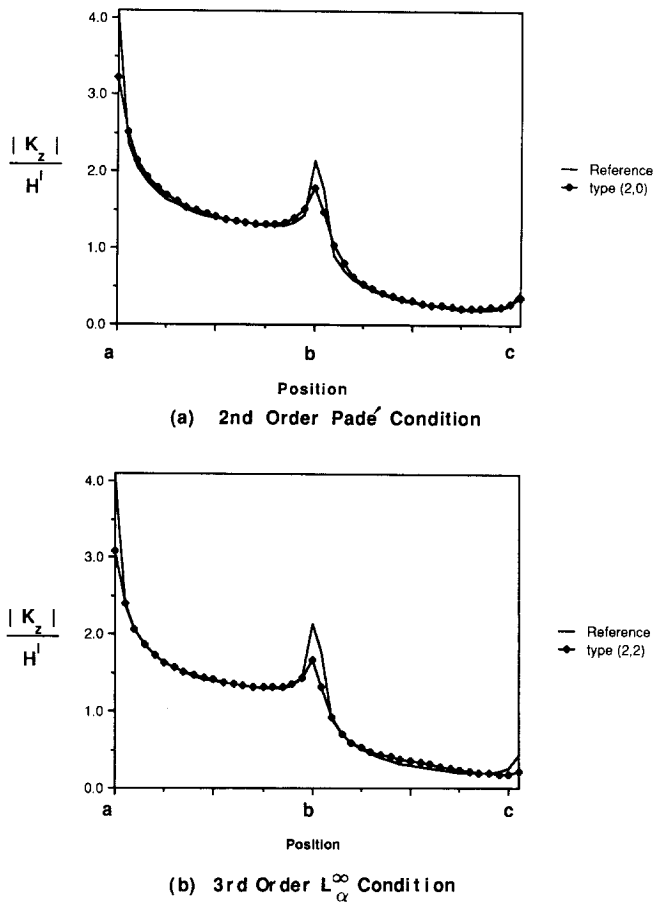

FIG. 21. Square cylinder, $\phi^i = 45°$, 50×50 grid.

ced significant cylindrical decay and spreading in reaching the boundary. It is well known that computational boundaries must be sufficiently distant from sources of scattered waves so that the boundary conditions operate on outward propagating plane waves. What is novel about our scattering experiments is the strong suggestion that second-order boundary conditions are preferable to third-order conditions on a small computational domain.

ACKNOWLEDGMENTS

We would like to thank Professor R. Higdon for his many helpful comments and suggestions provided during the review of this paper and Professor A. Bayliss for his support in the preparation of this paper. This work was supported in part by the National Science Foundation under Grant DMS-8700794.

REFERENCES

1. L. N. TREFETHEN AND L. HALPERN, *Math. Comput.* **47**, 421 (1986).
2. L. HALPERN AND L. N. TREFETHEN, Numerical Analysis Report 86-5, Dept. of Mathematics, Massachusetts Institute of Technology, 1986 (unpublished).
3. R. L. HIGDON, *Math. Comput.* **47**, 437 (1986).
4. K. S. YEE, *IEEE Trans. Antennas Propag.* **14**, 302 (1968).
5. A. TAFLOVE AND K. UMASHANKAR, *J. Electromagn. Waves Appl.* **1**, 363 (1987).
6. A. TAFLOVE AND K. UMASHANKAR, *IEEE Trans. Electromagn. Compat.* **25**, 433 (1983).
7. R. W. ZIOLKOWSKI, N. K. MADSEN, AND R. C. CARPENTER, *J. Comput. Phys.* **50**, 360 (1983).
8. A. R. MITCHELL, *Computational Methods in Partial Differential Equations* (Wiley, New York, 1969), p. 204.
9. B. ENGQUIST AND A. MAJDA, *Math. Comput.* **31**, 629 (1977).
10. G. MUR, *IEEE Trans. Electromagn. Compat.* **23**, 377 (1981).
11. G. A. KRIEGSMANN, A. N. NORRIS, AND E. L. REISS, *J. Acoust. Soc. Amer.* **79**, 1 (1986).
12. K. K. MEI AND J. VAN BLADEL, *IEEE Trans. Antennas Propag.* **11**, 185 (1963).
13. J. VAN BLADEL, *Electromagnetic Fields* (Hemisphere, New York, 1985), p. 388.
14. K. UMASHANKAR AND A. TAFLOVE, *IEEE Trans. Electromagn. Compat.* **24**, 397 (1982).
15. R. L. HIGDON, *Math. Comput.* **49**, 65 (1987).
16. B. ENGQUIST AND A. MAJDA, *Commun. Pure Appl. Math.* **32**, 313 (1979).
17. A. BAYLISS AND E. TURKEL, *Commun. Pure Appl. Math.* **33**, 707 (1980).